




# In situ SEM study of creep deformation behavior of nickel-based single-crystal superalloys

Wenling He<sup>1</sup>, Junxia Lu<sup>1,\*</sup> , Feiqi Li<sup>1</sup>, Wenxiang Jiang<sup>1</sup>, Jin Wang<sup>2</sup>, Yuefei Zhang<sup>2,\*</sup>, and Ze Zhang<sup>2</sup>

<sup>1</sup> Faculty of Materials and Manufacturing, Beijing University of Technology, Beijing 100124, China

<sup>2</sup> School of Materials Science and Engineering, Zhejiang University, Hangzhou 310027, China

Received: 2 March 2022

Accepted: 30 May 2022

Published online:  
8 July 2022

© The Author(s), under exclusive licence to Springer Science+Business Media, LLC, part of Springer Nature 2022

## ABSTRACT

This study aimed to compare the dynamic microstructure evolution and the creep mechanical properties of second-generation nickel-based single-crystal superalloys at 780 °C/720 MPa and 850 °C/720 MPa. A method based on in situ scanning electron microscopy creep testing was used to identify the occurrence of slip bands. At the same time, the deformation mechanisms at 780 °C and 850 °C were discussed. The creep life at 780 °C was longer, almost five times that at 850 °C. Moreover, significant necking occurred in the primary creep at 780 °C, which controlled the entire creep process and accounted for almost 50% of the total life. In comparison, the primary creep at 850 °C was obviously shortened, mainly showing the characteristics of the second and third stages; the necking was mainly concentrated in the later stage of creep. This difference must be caused by the dislocation motion. The slip deformation mainly occurred at 780 °C, and the  $\langle 112 \rangle$  dislocations shearing  $\gamma'$  strengthening phase left obvious slip bands on the surface. The dislocations moved in the matrix channel in the early stage of creep at 850 °C, and the dislocations sheared  $\gamma'$  strengthening phases in the later stage of creep while leaving obvious slip bands on the surface.

## Introduction

Nickel-based single-crystal superalloys have been extensively used in aero engine turbine due to their excellent creep and fatigue resistance at high temperatures. Second-generation nickel-based single-

crystal superalloys are now used as turbine blade materials in view of their stability under long-term service. However, centrifugal stress resulting from high-speed rotation can cause creep damage to fracture. Therefore, the creep property has become one of the main characteristics of nickel-based single-crystal superalloys [1, 2].

Handling Editor: Catalin Croitoru.

Address correspondence to E-mail: junxialv@bjut.edu.cn; yfzhang76@zju.edu.cn

<https://doi.org/10.1007/s10853-022-07397-0>

During service, different parts of the blade usually endure different temperatures and stresses. The root part of the blade is subjected to a low-temperature and high-stress environment, while the tail part is subjected to a high-temperature and low-stress environment. Mechanical properties and creep mechanisms show obvious differences in different temperature ranges [1, 3, 4]. According to different creep mechanisms, the creep behavior of nickel-based single-crystal alloys can be divided into three temperature ranges: the low-, middle-, and high-temperature creeps [2]. It is generally believed that in the high-temperature creep ( $T/T_m \geq 0.7$ ), dislocations move via climbing and cross-slip, and the microstructure presents an obvious rafting phenomenon [5–7]. In the middle-temperature creep ( $T/T_m \approx 0.6$ – $0.7$ ), dislocations in the matrix move mainly along  $\langle 110 \rangle$  direction without shearing the strengthening phase [8–10]. However, at low temperatures ( $T/T_m < 0.6$ ), the creep deformation mainly depends on dislocations by shearing the  $\gamma'$  strengthening phase coupled with various planar defect formations, for example, superlattice intrinsic or extrinsic stacking fault and antiphase boundary [11–14]. At low temperature and high stress, the creep tests are mainly controlled by the slip of  $\langle 112 \rangle$  dislocations [15–18].

Considering the fact that creep is extremely sensitive to temperature and stress, several studies reported its deformation mechanism. Dongqing Qi et al. [17] studied the microstructure of nickel-based single-crystal superalloys after creep at 760 °C/850 MPa and found that high-density stacking faults were formed in the  $\gamma'$  precipitate during the creep deformation process. The study of the [001] orientation of DD6 alloy under the creep condition of 760 °C/800 MPa showed that the  $\langle 112 \rangle$  dislocation ribbons could cut the  $\gamma$  and  $\gamma'$  phases at the same time and produce considerable primary creep [18]. Some researchers [19, 20] also found that dislocations were more likely to move in the matrix channel when the temperature was close to 850 °C. According to the report by Zhen-xue SHI et al. [19], under 850 °C/550 MPa creep condition, the lateral merging of  $\gamma'$  precipitates began along the direction of the applied stress. The shearing of  $\gamma'$  precipitation did not seem to be a creep deformation-controlling mechanism, and some dislocations were piled up in the  $\gamma$  matrix channel and the interfacial regions of the  $\gamma/\gamma'$  phase. Indeed, in the well-cited paper of Pollock and Argon

[20], which dealt with the creep deformation behavior of CMSX-3 at 825 °C/450 MPa, no stacking fault shear was reported: the dislocations propagated from grown-in dislocations looping through the channels between the  $\gamma'$  precipitates. Nevertheless, since the aforementioned studies used non-in situ methods, the influence of the movement of dislocations on the evolution of the microstructure and the creep performance is still unclear so far. The in situ research method could dynamically observe the process of microstructure evolution in the creep process in real time, which solved the aforementioned problems. In recent years, the research team used a self-designed in situ high-temperature tensile test platform combined with scanning electron microscopy (SEM) to examine the tensile deformation behavior of Ti6Al4V alloy and nickel-based alloy [21–25].

Based on the high-temperature in situ tensile equipment developed by the research group in the early stage, the low temperature and high-stress in situ creep tests were performed in this study. Also, the microstructure evolution during the creep tests of the second-generation nickel-based single crystal at 780 °C/720 MPa and 850 °C/720 MPa was observed. In this study, the occurrence of necking at two temperatures was observed, and its effect on creep properties was analyzed. In addition, the difference in creep mechanism was intrinsically related to the dislocation motion. In this study, the invisible dislocation behavior was related to the surface slip bands, and the different creep mechanisms at two temperatures were explored.

## Materials and methods

### Sample preparation

The second-generation nickel-based single-crystal superalloy with [001] orientation was prepared by directional solidification and crystal selection. The nominal chemical composition was Cr 4.3, Co 9.1, W 8, Al 5.2, Ta 6, Re 2.5, Mo 1.5, Hf 0.1, and Nb 0.5 (wt.%), and balanced by Ni. The single crystal was treated as follows: 1290 °C/1 h + 1300 °C/2 h + 1318 °C/6 h, air cooling (AC) + 1130 °C/4 h, AC + 870 °C/32 h, AC. In this study, the orientation deviation of the material from standard [001] was determined to be less than 10° using the electron backscatter diffraction (EBSD) technique. The

samples for the creep test were then cut using the electric discharging machining technique at the dimensions shown in Fig. 1a. Figure 1a shows the sample with a gauge of  $2 \times 2 \text{ mm}^2$  and a thickness of 0.7 mm. The loading direction was [001], and the normal direction of the observation plane was [010].

Before creep testing, the samples were mechanically ground with SiC abrasive papers until no obvious scratches were found on the surface. Then, the samples were polished using a diamond water-soluble polishing paste with a particle diameter of  $0.5 \mu\text{m}$  until the mirror was smooth. Subsequently, the electrochemical polishing was executed with a constant-current mode (1.4 A, about 31 V, 10 s) in the electrolyte of  $\text{HClO}_4\text{:C}_2\text{H}_5\text{OH} = 1\text{:}9$  (volume ratio). The samples were then cleaned with alcohol and dried at room temperature for about 5 min. A solution of  $\text{CuSO}_4\text{:HCl:H}_2\text{O} = 4 \text{ g:}20 \text{ mL:}20 \text{ mL}$  was used as chemical etching for 2 s for the SEM metallography studies.

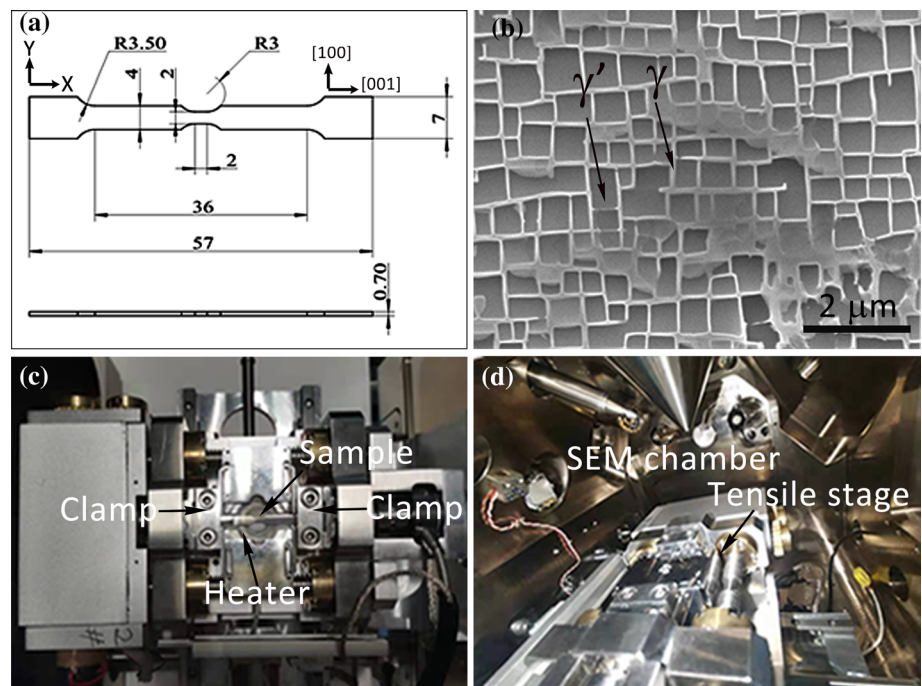
Figure 1b shows the microstructure of a single-crystal superalloy. The white  $\gamma$  matrix phase separated the dark  $\gamma'$  strengthening phase, and the two phases were neatly arranged in the material. The size and volume fraction of the  $\gamma'$  phase were 420 nm and 66%, respectively, which were calculated using ImageJ software. In addition, the material also had some casting defects such as pores and eutectics.

### In situ SEM creep testing

In this study, the in situ tensile testing system was used for creep tests, which was independently developed by the research group. The system integrated both the tensile stage and the heater, as shown in Fig. 1c. During the experiment, the sample was clamped and fixed at both ends of the tensile stage. The load was applied through the rotation of the gear driven by the motor. The limited load of the system was 2500 N. The heater was placed under the sample with the limited heating temperature of  $1200 \text{ }^\circ\text{C}$ . The inside of the heater was a tungsten wire, and the temperature was controlled by adjusting the voltage to control the heating of tungsten wire. The temperature of the lower surface of samples was monitored using a K-type thermocouple. Figure 1d shows the picture of tensile stage installed into the SEM (TESCAN S8000). The exerted temperature and load were controlled using the software matched with the tensile stage.

The creep experiments were executed at  $780 \text{ }^\circ\text{C}/720 \text{ MPa}$  and  $850 \text{ }^\circ\text{C}/720 \text{ MPa}$ . Before the creep experiment, the sample was scanned with EBSD to obtain the Euler angle, which was convenient for calculating the slip. The experimental parameters were 20 keV, 1 nA, and WD 15 mm. After that, the sample and the tensile stage were installed, as shown

**Figure 1** **a** Samples size (unit: mm); **b** microstructure; **c** the in situ setup of the creep testing; and **d** tensile testing stage mounted on the SEM sample stage.



in Fig. 1c, and it was tested whether it could be heated and applied stress normally by applying a small voltage of about 0.5 V and a small stress of 20 MPa. The stretching system was then fixed in the SEM, followed by heating. The temperature was slowly increased by adjusting voltage with the increment of 0.5 V. The force was applied to the target stress only after reaching the target temperature and holding for 30 min. Since then, the creep experiment was timed. In this study, the creep strain was obtained by recording the length change of two marks on the sample surface and then converting it into strain using Formula (1).

$$\varepsilon = \frac{L - L_0}{L_0} \tag{1}$$

where  $L_0$  is the initial length of the marks, and  $L$  is the real-time length.

Once the creep began, the initial length  $L_0$  was recorded, based on which the creep strain was measured. During the entire creep testing process, the temperature and stress were controlled within the error of < 5%, and it was considered that the constant-temperature and constant-stress conditions required by the creep test were met. During the experiment, the marks were recorded every 10 min, and the new phenomena on the surface of the sample were recorded at any time. The creep experiment ended when the sample ruptured.

### Methodology for determining slip trace and Schmid factor

Slip trace is defined as a straight line resulting from the intersection of an active slip plane and the sample surface. In this study, the orientation of the slip trace was represented by the  $\theta$  angle between the slip trace and the axial stress. It was expressed as:

$$\cos \theta = \frac{(n \times N) \cdot T}{|n \times N||T|} \tag{2}$$

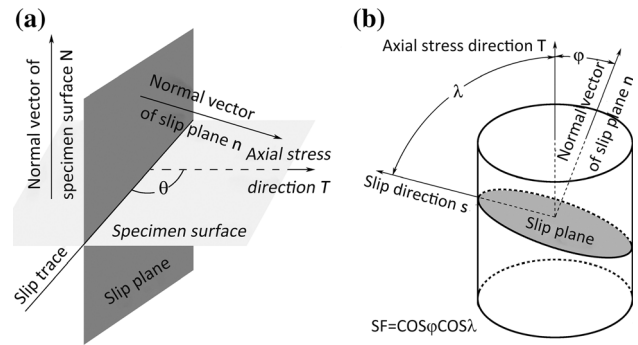


**Figure 2** a Schematic showing the slip trace; b calculation method for the Schmid factor.

The physical quantities in Formula (2) are shown in Fig. 2a.

Schmid factor reflects the magnitude of resolved shear stress on a slip system, was calculated as follows:

$$SF = \frac{(n \cdot T) \cdot (s \cdot T)}{|n||s||T|^2} \tag{3}$$

The physical quantities in Formula (3) are shown in Fig. 2b. In Formulas (2) and (3), the vectors with lowercases, that is,  $n$  and  $s$ , represent crystal coordinate systems, corresponding to the Miller index of the slip plane and slip direction in a slip system, respectively. The vectors with uppercases, that is,  $N$  and  $T$ , represent coordinate systems of samples. In this study,  $N$  and  $T$  were along the  $z$ -axis and  $x$ -axis of the sample coordinate system, respectively. It should be noted that the vectors in different coordinate systems cannot be directly operated. Therefore, these vectors should be unified in the same coordinate system before the operation.

The coordinate transformation matrix  $g$  from the sample coordinate system to the crystal coordinate system is related to the Euler angle, that is,  $(\phi_1, \phi, \phi_2)$ , obtained using EBSD scanning before the creep experiment. It can be expressed as follows [26]:

$$g = \begin{cases} \cos \phi_1 \cos \phi_2 - \sin \phi_1 \sin \phi_2 \cos \phi & \sin \phi_1 \cos \phi_2 + \cos \phi_1 \sin \phi_2 \cos \phi \sin \phi_2 \sin \phi \\ -\cos \phi_1 \sin \phi_2 - \sin \phi_1 \sin \phi_2 \cos \phi - \sin \phi_1 \cos \phi_2 + \cos \phi_1 \sin \phi_2 \cos \phi \cos \phi_2 \sin \phi \\ \sin \phi_1 \sin \phi - \cos \phi_1 \sin \phi \cos \phi \end{cases} \tag{4}$$

In fact, 24 solutions exist for  $g$  in cubic symmetry because of 24 different ways in which a crystal with cubic symmetry can be arranged [26]. In this study, it was specified that the directions [001], [100], and [010] of the crystal coordinate system were the closest to the  $x$ -,  $y$ -, and  $z$ -axes of the sample coordinate system, respectively. In this way,  $g$  could be uniquely determined. Consequently, Formulas (2) and (3) should be replaced by:

$$\cos \theta = \frac{(n \times N^t) \cdot T^t}{|n \times N^t||T^t|} \tag{5}$$

$$SF = \frac{(n \cdot T^t) \cdot (s \cdot T^t)}{|n||s||T^t|^2} \tag{6}$$

Among these,

$$\begin{cases} N^t = g \cdot N \\ T^t = g \cdot T \end{cases} \tag{7}$$

Before the experiment, nine points were randomly selected within the gauge section of the sample. Their orientations represented by Euler angles were acquired using EBSD, and are shown in the form of a pole figure in Fig. 3a. It was found that the original orientation at each point did not accord with the selection of the crystal coordinate system. Therefore, to each point, 24 solutions for  $g$  needed to be listed to determine the exact one. It was accomplished by pre-multiplying the original  $g$  by 24 symmetry operators, which is included in Appendix II of reference [26]. The modified orientations of these points are shown in Fig. 3b. Based on the modified crystal orientations of the nine points, the average values of  $\theta$  and Schmidt factor (SF) of a specific slip system could be calculated.

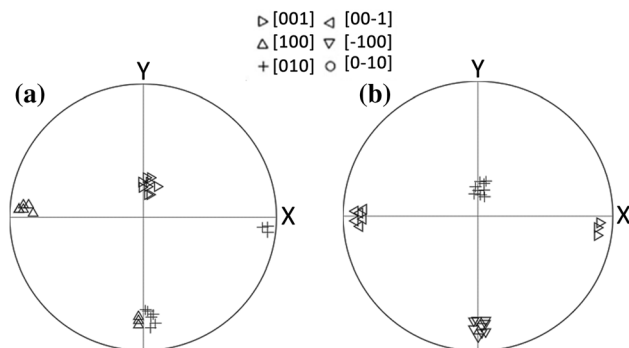


**Figure 3** a Original and b modified orientations of randomly distributed nine points within the gauge section.

## Results

### Creep properties

The creep properties of the single-crystal superalloy were investigated at 780 °C and 850 °C with a stress of 720 MPa. After the creep experiment started, two eutectic defects on the sample surface were selected as the marks used to measure the distance change during the in situ creep, which are shown in Fig. 4a; the magnified picture is shown in Fig. 4b. By recording the length change between the two marks, the relationships between the strain and time at 780 °C and 850 °C are shown in Fig. 4c. It was found that the single-crystal superalloy showed different creep properties at two temperatures. At 850 °C, the creep life was smaller and the creep rate was faster than that at 780 °C. The strain of the two samples before fracture was about 20%. At 780 °C, the creep life was close to 5 h, which was about five times that at 850 °C. For the creep time duration of 1 h, the strain at 780 °C was about 3%, whereas that at 850 °C was about 18%. These findings implied that the creep rate increased and life reduced with the increase in temperature under the same-stress condition. Similar results were reported for CMSX-4 and other nickel-based single-crystal superalloys [15, 27].

By fitting the time–strain curves, the results are shown in Fig. 5a at 780 °C and Fig. 5c at 850 °C. When the first-order differentia was taken to the strain of the sample at two temperatures, the strain rate curves were obtained; the curve at 780 °C is shown in Fig. 5b and that at 850 °C is shown in Fig. 5d. From the two graphs, it was deduced that the strain rate had a large difference. According to the inflection points of the strain rate, the creep process could be divided into incubation, primary, secondary, and tertiary creeps. The solid points

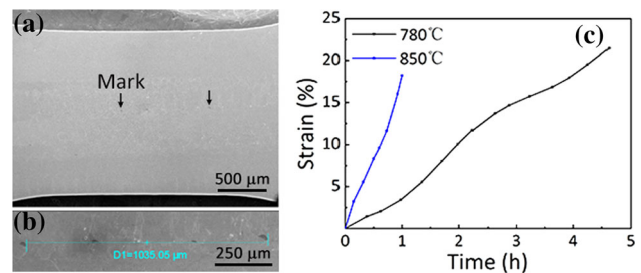


**Figure 4** a Position of marker points; b marker point measurement; and c time–strain curves of in situ creep tests at 780 °C and 850 °C (tensile axis is along the horizontal direction).

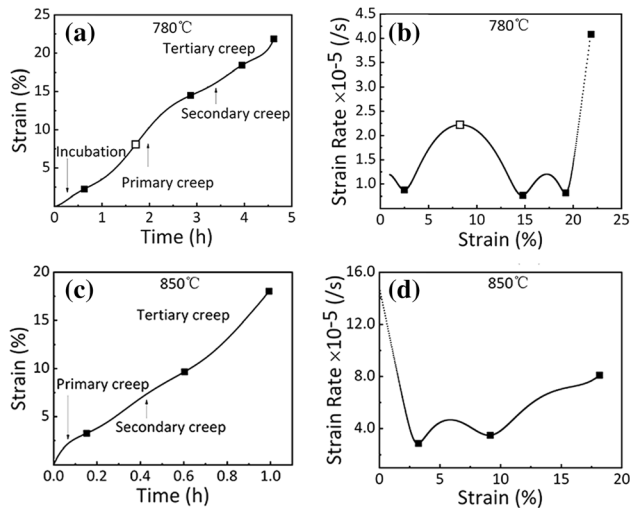


**Figure 5** 780 °C: **a** Time–strain curve; **b** strain–strain rate curve; 850 °C: **c** time–strain curve; and **d** strain–strain rate curve.

represented the end of each stage, and the hollow point denoted the transition from the acceleration to the deceleration period of the primary creep. It was found that at 780 °C, the sample experienced incubation during the initial 0.5 h with a nearly stable creep rate. After that, the creep rate changed dramatically with the rapid increase and decrease until the duration of 3 h entering the stable stage. After 4 h, the creep rate increased again until the fracture of the sample. As a comparison, at 850 °C, the creep directly entered the primary stage without incubation, where the creep rate decreased rapidly. Literatures also reported the similar results in nickel-based single crystal superalloys [20, 28]. They found that the duration of incubation decreased with the temperature increasing under the same stress. Pollock et al. found the duration of incubation period of CMSX-3 nickel-based single crystal superalloy at 800 °C is  $1.6 \times 10^4$  s, and 600 s at 850 °C. While at 900 °C, it is very short and unable to accurately measure [20]. After about 0.15 h, the creep rate was basically unchanged, which was the steady-state stage. In 0.6 h, it entered the third stage of the increasing rate.

**Table 1** Strain in each stage and the ratio of duration in each stage to the total life

Temperature		Incubation	Primary creep	Secondary creep	Tertiary creep
780 °C	Strain (%)	2.11	14.36	18.25	21.85
	Life ratio (%)	13.42	48.70	22.94	14.94
850 °C	Strain (%)	\	3.24	9.62	18.22
	Life ratio (%)	\	15.25	44.01	40.68

The strain in each stage and the ratio of duration in each stage to the total life are listed in Table 1. It was found that the cumulative strain in the primary creep at 780 °C was the largest, about 12.25% (primary creep strain minus incubation strain), and the duration was the longest, close to 48.7%, compared with other stages. Therefore, it was deferred that the primary creep dominated the entire creep process at 780 °C. In contrast, at 850 °C, the primary creep strain was only 3.24%, and the duration accounted for about 15.25% of the total life. The main creep accumulation occurred in the tertiary stage and accounted for 40.68% of the total life. Similar results were obtained in the CMSX-4 alloy; the primary creep strain at 850 °C/750 MPa was about 2.9%, while the primary creep strain at 750 °C was significantly larger, about 6.3% [15, 16]. At a medium temperature, the alloy exhibited a continuous softening process with an increasing rate in the third stage [3, 29]. Therefore, the creep of the single-crystal alloy was the low-temperature creep at 780 °C and was close to the medium-temperature creep at 850 °C.

### In situ macroscopic creep deformation process at 780 °C and 850 °C

Figure 6 shows the in situ macroscopic deformation process of the sample at 780 °C. Compared with the macrostructure before creep shown in Fig. 6a, the sample entered the primary creep acceleration period, as shown in Fig. 6b, under the creep strain of 6.13%, and the width of the gauge segment was reduced from 1902.06 to 1896.33  $\mu\text{m}$ . Only slight necking occurred in this stage. Until the creep strain was close to 14.32%, that is, the end of the primary creep, the gauge length section was significantly elongated. Obvious necking was observed on the surface of the sample, and the width of the gauge segment was further reduced to 1793.84  $\mu\text{m}$ , as shown in Fig. 6c. Notably, the significant necking had already occurred in the primary creep, resulting in a short duration of the secondary and tertiary creeps,

**Figure 6** In situ macroscopic deformation process at 780 °C: **a** before creep; **b** for 6.13%; and **c** for 14.32% (the tensile axis was along the horizontal direction).

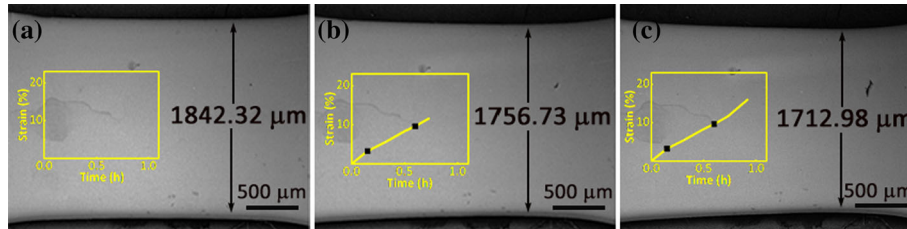
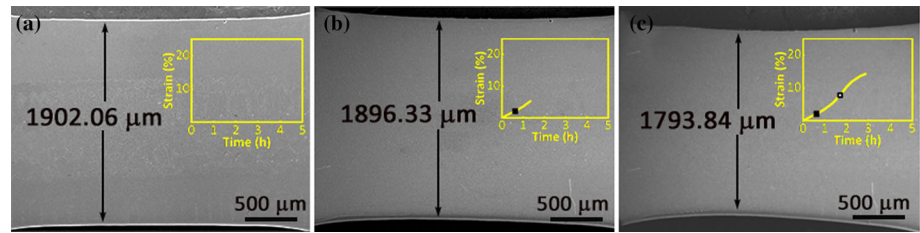


**Figure 7** In situ macroscopic deformation process in different stages at 850 °C: **a** before creep; **b** for 11.63%; and **c** for 16.04% (the tensile axis was along the horizontal direction).

which was the longest in the primary creep of the entire creep process, as shown in Fig. 5a.

The in situ macroscopic deformation at 850 °C creep conditions is shown in Fig. 7. In the primary creep stage, only the axial elongation occurred on the surface of the sample. When the creep strain was close to 11.63%, that is, the secondary stage ended (Fig. 7b), the right side of the sample surface was necked, and the width reduced from 1842.32 to 1756.73 μm. In the third stage, the gauge length section was further necked, and the width reduced to 1712.98 μm (Fig. 7c). Similar to 780 °C, obvious necking occurred at 850 °C. It was worth noting that necking occurred in the later stage of creep (the second and third stages), as shown in Fig. 7. In the 850 °C creep test, the primary creep was very short, accounting for only 15.25% of the total life. The later stage of the creep was accompanied by necking, resulting in a higher creep rate and lower creep life.

**In situ microscopic creep deformation process at 780 °C and 850 °C**

The macroscopic deformation process was closely related to the evolution of the microstructure. Slip deformation was most likely to occur at low temperatures, and the activation of the slip system was related to the size of the SF. It was generally believed that the larger the SF, the easier the slip system to activate. Therefore, it was necessary to calculate the SF for judging the activation of the slip system. The size of the SF was calculated using Euler angles. At

the same time, the Euler angles could also predict the direction of the slip band ( $\theta$ ) left on the sample surface after the slip system was activated. The relationship was introduced in ‘Methodology for determining slip trace and Schmid factor’ section. In this study, the Euler angles were obtained from the EBSD characterization of the sample before the creep. The single-crystal alloy used in this study was a face-centered cubic structure with the {111} close-packed plane and the  $\langle 110 \rangle$  close-packed direction. It was inferred that the  $\langle 110 \rangle$  direction was the original dislocation direction. Rae [30] also confirmed the opinion using transmission electron microscope characterization for a nickel-based single crystal. However, usually, a large number of  $\langle 112 \rangle$  dislocations were observed at high temperatures, which were generated by the dislocation reaction with  $\langle 110 \rangle$  dislocations [31]:

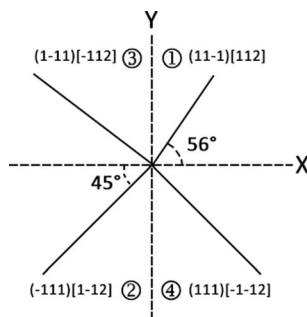
$$a/2[-101] + a/2[011] \rightarrow a/3[-112] + a/6[-112] \tag{8}$$

Based on the aforementioned deduction, the slip direction of the single-crystal alloy was  $\langle 110 \rangle$  or  $\langle 112 \rangle$ . To decide the exact slip system, it was necessary to calculate the SF of the 24 slip systems included in {111}  $\langle 110 \rangle$  and {111}  $\langle 112 \rangle$ .

The calculated results of the SF for the creep experiment at 780 °C are shown in Table 2. It was found that the SF of the  $\langle 112 \rangle$  dislocations was higher. More importantly, the critical shear stress of the  $\langle 112 \rangle$  dislocation was lower than that of the  $\langle 110 \rangle$  dislocation; therefore, the former was

**Table 2** Calculation statistics of Schmidt factor (SF) of 24 slip systems at 780 °C

Slip system		Schmidt factor	Slip system		Schmidt factor
(111)	[0-11]	0.367210	(111)	[-1-12]	0.435955
(111)	[-101]	0.387887	(111)	[1-21]	0.200071
(111)	[-110]	0.020677	(111)	[-211]	0.235885
(-111)	[0-11]	0.441308	(-111)	[1-12]	0.480014
(-111)	[101]	0.390101	(-111)	[12-1]	0.284353
(-111)	[110]	0.051207	(-111)	[211]	0.195661
(1-11)	[011]	0.369423	(1-11)	[-112]	0.452904
(1-11)	[-101]	0.415030	(1-11)	[121]	0.186956
(1-11)	[110]	0.045606	(1-11)	[21-1]	0.265948
(11-1)	[011]	0.439033	(11-1)	[112]	0.491850
(11-1)	[101]	0.412816	(11-1)	[-121]	0.268682
(11-1)	[-110]	0.026278	(11-1)	[2-11]	0.223168



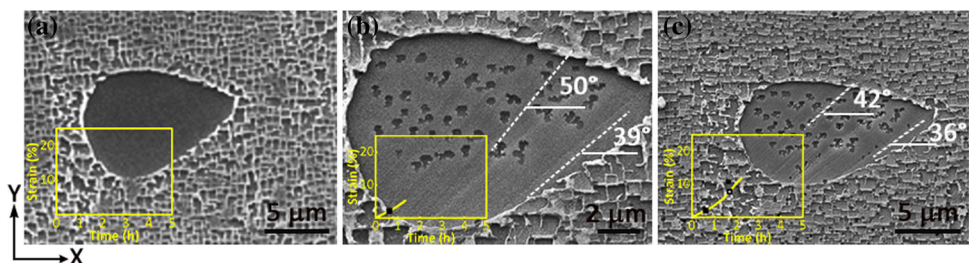
slip system	SF
(11-1)[112]	0.491850
(-111)[1-12]	0.480014
(1-11)[-112]	0.452904
(111)[-1-12]	0.435955

**Figure 8** Slip systems with a higher Schmidt factor and the direction of the slip bands at 780 °C.

easier to shear the  $\gamma'$  strengthening phase [32]. Thus, the slip bands on the sample surface resulted from the shear  $\gamma'$  strengthening phase of the  $\langle 112 \rangle$  dislocations. Figure 8 shows the slip systems with higher SF and the direction of the slip bands. It was found that the first to be activated were the slip systems (11-1)[112] and (-111)[1-12], which were, respectively, 56° and 45° with the stress axis.

During the experiment, the occurrence of slip deformation was first observed near the necking area. Its microstructure evolution process is shown in Fig. 9. Obvious slip bands were found in the area close to the necked area. When the strain reached

5.36%, it was in the primary creep of acceleration (Fig. 9b). Slip bands were noted approximately 50° and 39° from the stress axis, and the density of the slip bands in the 50° direction was greater. The density of the slip bands increased continuously, and at the primary creep of deceleration (Fig. 9c), its direction changed to 42° and 36°, respectively, which was the inevitable result of continuous creep stretching. The direction of the slip bands observed on the surface of the sample (Fig. 9b) was slightly smaller than the calculated result. This was because the slip bands were not recorded when they first appeared, and the direction of the slip bands shown in Fig. 9b resulted from continuous creep stretching. Therefore, we concluded that the slip bands observed on the surface of the sample during the creep process were consistent with the calculated results, which also showed that this material followed the SF principle. In addition, obvious slip bands were found in the eutectic during the experiment, but the complete two phases did not appear. This was caused by the excessively deep corrosion of the strengthening phase during sample preparation. The surface of the two phases was not flat, and the size was much smaller

**Figure 9** Evolution process of the microstructure before the end of the primary creep at 780 °C: **a** before creep; **b** for 5.36%; and **c** for 11.98% (the tensile axis was along the horizontal direction).



**Table 3** Calculation statistics of Schmidt factor (SF) of 24 slip systems at 850 °C

Slip system		Schmidt factor	Slip system		Schmidt factor
(111)	[0–11]	0.375850	(111)	[–1–12]	0.447768
(111)	[–101]	0.399706	(111)	[1–21]	0.203224
(111)	[–110]	0.023856	(111)	[–211]	0.244544
(–111)	[0–11]	0.436087	(–111)	[1–12]	0.482817
(–111)	[101]	0.400270	(–111)	[12–1]	0.272454
(–111)	[110]	0.035817	(–111)	[211]	0.210417
(1–11)	[011]	0.376414	(1–11)	[–112]	0.452828
(1–11)	[–101]	0.407908	(1–11)	[121]	0.199140
(1–11)	[110]	0.031494	(1–11)	[21–1]	0.253689
(11–1)	[011]	0.435523	(11–1)	[112]	0.486630
(11–1)	[101]	0.407344	(11–1)	[–121]	0.267719
(11–1)	[–110]	0.028179	(11–1)	[2–11]	0.218911

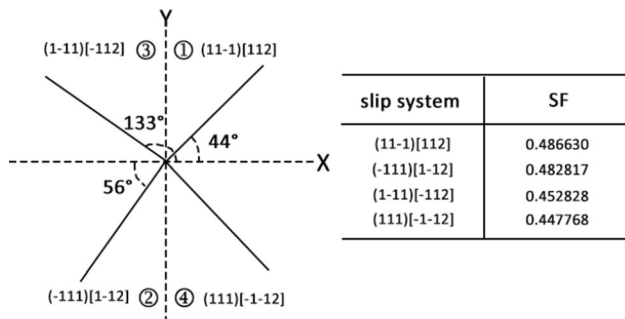


**Figure 10** Slip systems with a higher Schmidt factor and the direction of the slip bands at 850 °C.

than that of the eutectic. Therefore, it was difficult to observe obvious slip bands.

At 850 °C, the SF and the direction of the possible slip bands on the surface were also calculated, as shown in Table 3 and Fig. 10. The microstructural evolution process near the necked region where slip deformation occurred first is shown in Fig. 11. The calculation results showed that the slip systems (–111)[1–12] and (11–1)[112] were activated first, and the corresponding slip band directions were, respectively, 56° and 44° with the stress axis; the latter had a larger SF. Figure 11a shows that no obvious slip band

was observed in the early stage of creep. When the creep strain was 17.04% in the third stage, slip bands approximately 53° and 41° with the stress axis were found on the surface, and the 41° direction was denser, as shown in Fig. 11b. This result was quite similar to the calculated slip band directions of 56° and 44°, as shown in Fig. 10. The calculation results also showed that the SF of the (1–11)[–112] slip system ranked third, and the direction of the slip band was 133°. Similarly, a slip band of about 134° appeared on the surface of the sample when it was close to the fracture (Fig. 11c). At this temperature, the sequence and direction of the slip bands on the sample surface were consistent with the calculated results.

### Discussion

This section will discuss the creep deformation mechanism at 780 °C and 850 °C in detail. The model diagram of dislocation evolutions and main deformation mechanisms are shown in Fig. 12. Figure 9b shows obvious slip bands on the surface during the primary creep of acceleration in the 780 °C creep test;

**Figure 11** Evolution process of the microstructure close to the necked area at 850 °C for: **a** 8.35%, **b** 17.04%, and **c** fracture (the tensile stress axis is along the horizontal direction).

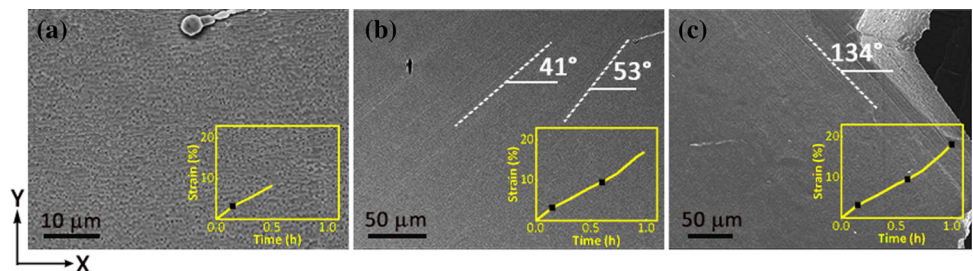
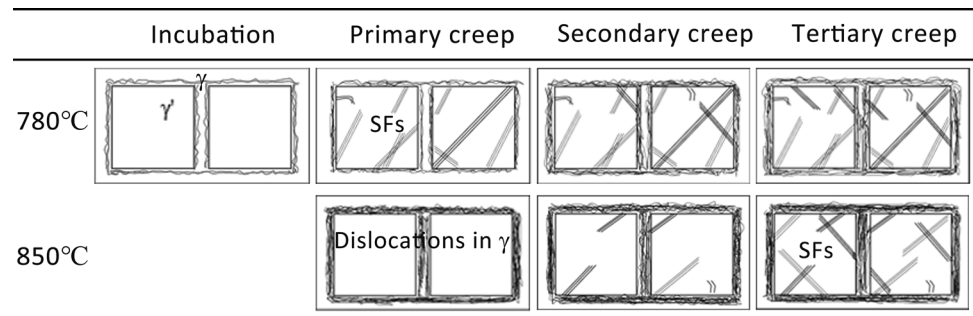
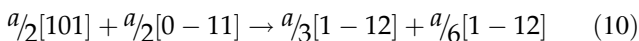
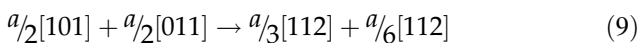


**Figure 12** Schematic illustration of deformation mechanisms at 780 °C and 850 °C.



it was the result of activation of the (11-1)[112] and (-111)[1-12] slip systems, as shown in Fig. 8. Thus, the [112] and [1-12] dislocations were generated during the incubation period. During this period,  $\langle 110 \rangle$  dislocations proliferated and propagated in the matrix channels, generating a sufficient number of  $\langle 112 \rangle$  dislocations from the following reactions [31]:



The primary creep deformation is associated with the propagation of  $\langle 112 \rangle$  dislocations, which are able to cut through both  $\gamma$  and  $\gamma'$  phases until interacting with other dislocations [15, 18]. During  $\langle 112 \rangle$  dislocation shearing  $\gamma'$  strengthening phase, the accompanied stacking fault will hinder dislocation movement and contribute to work hardening of materials [33, 34]. However, when the applied stress exceeds the threshold stress, large number of  $\langle 112 \rangle$  dislocations will cut through the strengthening phase. The threshold stress of the CMSX-4 s-generation nickel-based single crystal superalloy at 750 °C is 530 MPa. From TEM results, it also shows a large number of stacking faults in the primary creep at 750 MPa [15]. In addition, the  $\langle 112 \rangle$  dislocation cutting through strengthening phase is a movement and propagation process of dislocations. Literature reported that in the early stage of primary creep,  $\langle 112 \rangle$  dislocations move in a long distance and the strain rate increases rapidly as the nucleation of mobile  $\langle 112 \rangle$  dislocations increases [12]. From Fig. 9b, slip bands were obviously formed on the surface at the acceleration period of primary creep due to  $\langle 112 \rangle$  dislocations movement by slip and shearing the  $\gamma'$  strengthening phase. Therefore, during the primary creep acceleration period, the distance of the  $\langle 112 \rangle$  dislocation

movement is relatively long, and a large number of  $\langle 112 \rangle$  dislocations were nucleated and propagated through the  $\gamma$  and  $\gamma'$  phases, resulting in an increase in the creep rate. At the same time, according to the calculation result of SF, the  $\langle 110 \rangle$  dislocation were close to 4.3, thus the APB coupled dislocation pairs may also existed in  $\gamma'$  phase. The decrease in the creep rate in the primary creep was due to work hardening. In general, two sources existed for work hardening. One was that the formation of dense dislocation networks at  $\gamma/\gamma'$  interface. The other was the interactions between the two  $\{111\} \langle 112 \rangle$  slip systems [15, 35]. As shown in Fig. 9b, already two deformation bands existed on the surface during the primary creep of acceleration, along the 50° and 39° directions, respectively, indicating that at least two  $\{111\} \langle 112 \rangle$  slip systems were activated at this time. Therefore, for the 780 °C creep test, the effect of interaction between (11-1)[112] and (-111)[1-12] slip systems might be the major reason for work hardening, which resulted in a decrease in the creep rate. No significant change was found in the creep strain rate in the secondary creep, as shown in Fig. 5b, which resulted from the equilibrium of work hardening and recovery softening mechanisms. As shown in Fig. 6c, the surface of the sample in the primary creep was significantly necked. The intensification of the necking phenomenon led to an increase in the real stress, which broke the dynamic balance, and the creep strain rate continued to increase until it broke.

The creep deformation mechanism of 850 °C was very different from that of 780 °C. As shown in Eqs. (8), (9), (10), in order to combine to form  $\langle 112 \rangle$  dislocations, the two  $\langle 110 \rangle$  dislocation with Burgers vectors of 60° meet in a common  $\{111\}$  slip plane by dislocation slip and climb [13]. At 850 °C, more vacancies were formed than those at 780 °C, which provided the chance for dislocation movement. The accelerated movement

of  $\langle 110 \rangle$  dislocations in the matrix channel shortened the encounter time, resulting in short incubation. As shown in Fig. 5, there was no obvious incubation at 850 °C. A large number of dislocations moved in the matrix channel and entangle each other, resulting in a decrease in the creep strain rate in the primary creep. In the primary creep, although the  $\langle 112 \rangle$  dislocations can nucleate, they were hindered by a large number of  $\langle 110 \rangle$  dislocations in the matrix channel and cannot sheared the  $\gamma'$  strengthening phase. The dislocations tend to moved in the matrix channel, and no slip bands were observed on the surface of the specimen. Same as at 780 °C, the mechanism of recovery softening and work hardening in the secondary creep reached a dynamic balance. At the same time, the surface was necked in this stage and the real stress increased, hence, the  $\langle 112 \rangle$  dislocation might have a small amount of cut into the strengthening phase. However, the surface slip bands resulted from the accumulated deformation of many dislocations. Therefore, no obvious slip band was noted on the surface, as shown in Fig. 11a. In the tertiary stage, severe necking occurred on the surface of the sample, as shown in Fig. 7c, which caused the true stress to increase significantly. The slip systems  $(-111)[1-12]$ ,  $(11-1)[112]$ , and  $(1-11)[-112]$  were activated, and the  $\gamma'$  strengthening phase was largely sheared, with obvious slip bands in the necked area, as shown in Fig. 11b and c. The  $[1-12]$ ,  $[112]$ , and  $[-112]$  dislocations were generated by the dislocation reactions (9), (10), and (8), respectively.

## Conclusions

The in situ creep experiment using the scanning electron microscope was employed to study the mechanical properties and microstructure evolution process under the same-stress and different-temperature creep conditions of 780 °C/720 MPa and 850 °C/720 MPa. This study linked the invisible dislocation behavior to the microstructure evolution observed in real time on the surface, and explored the effect of temperature on creep deformation. The conclusions were as follows:

1. In the same-stress creep test, the higher the temperature, the faster the creep rate and the shorter the creep life.
2. The slip deformation mainly occurred at 780 °C, and the  $\langle 112 \rangle$  dislocation sheared the  $\gamma'$  strengthening phase to generate stacking faults. At a higher temperature of 850 °C, dislocations moved in the matrix channel in the early stage of creep, and dislocations cut the  $\gamma'$  strengthening phase in the later stage of creep, leaving obvious slip bands on the surface of the sample.
3. For the 780 °C creep test, the sample surface had already undergone significant necking in the primary creep, which controlled the creep process. However, the surface necking of the 850 °C creep test was concentrated in the later stage of the creep.

## Acknowledgements

This research was funded by National Science and Technology Major Project of China(J2019-III-0008-0051), Basic Science Center Program for Multiphase Media Evolution in Hypergravity of the National Natural Science Foundation of China (No: 51988101) and Key projects of Beijing Natural Science Foundation (KZ202110005006).

## Declarations

**Conflict of interest** The authors declare that they have no conflict of interest.

## References

- [1] Pollock TM, Tin S (2006) Nickel-based superalloys for advanced turbine engines: chemistry, microstructure and properties. *J Prop Power* 22:361–374
- [2] Reed RC (2006) The superalloys: fundamentals and applications. Cambridge University Press, New York
- [3] Reed RC, Matan N, Cox DC, Rist MA, Rae CMF, Univ OCRU (1999) Creep of CMSX-4 superalloy single crystals: effects of rafting at high temperature. *Acta Mater* 47:3367–3381
- [4] Matan N, Cox DC, Carter P, Rist MA, Rae CMF, Reed RC (1999) Creep of CMSX-4 superalloy single crystal: effects of misorientation and temperature. *Acta mater* 47:1549–1563
- [5] Touratier F, Andrieu E, Poquillon D, Viguier B (2009) Rafting microstructure during creep of the MC2 nickel-based superalloy at very high temperature. *Mater Sci Eng A* 510–511:244–249

- [6] Alain J, Roxane T, Thomas S (2018) High-temperature dislocation climb in the  $\gamma'$  rafts of single-crystal superalloys: the hypothesis of a control by dislocation entry into the rafts. *Metall Mater Trans A* 49:4110–4125
- [7] Chiou MS, Jian SR, Yeh AC, Kuo CM, Juang JY (2016) High temperature creep properties of directionally solidified CM-247LC Ni-based superalloy. *Mater Sci Eng A* 655:237–243
- [8] Wollgramm P, Buck H, Neuking K, Parsa AB, Schuwalow S, Rogal J, Drautz R, Eggeler G (2015) On the role of re in the stress and temperature dependence of creep of Ni-base single crystal superalloys. *Mater Sci Eng A* 628:382–395
- [9] Coakley J, Reed RC, Warwick JLW, Rahman KM, Dye D (2012) Lattice strain evolution during creep in single-crystal superalloys. *Acta Mater* 60:2729–2738
- [10] Xia W, Zhao X, Yue L, Zhang Z (2020) Microstructural evolution and creep mechanisms in Ni-based single crystal superalloys: a review. *J Alloy Compd* 819:152954
- [11] Long HB, Liu YN, Kong DL, Wei H, Chen YH, Mao SC (2017) Shearing mechanisms of stacking fault and anti-phase-boundary forming dislocation pairs in the  $\gamma'$  phase in Ni-based single crystal superalloy. *J Alloy Compd* 724:287–295
- [12] Rae CMF, Matan N, Reed RC (2001) The role of stacking fault shear in the primary creep of [001]-oriented single crystal superalloys at 750 °C and 750 MPa. *Mater Sci Eng A* 300:125–134
- [13] Wu X, Dlouhy A, Eggeler YM, Spiecker E, Kostka A, Somsen C, Eggeler G (2017) On the nucleation of planar faults during low temperature and high stress creep of single crystal Ni-base superalloys. *Acta Mater* 144:642–655
- [14] Dang CX, Zhang P, Li J, Gao ZH, Li B, Gong XF, Song XL (2020) The role of  $\langle 112 \rangle\{111\}$  slip in the initial plastic deformation of Ni-base superalloys at room temperature. *Mater Charact* 170:110648
- [15] Rae CMF, Reed RC (2007) Primary creep in single crystal superalloys: origins, mechanisms and effects. *Acta Mater* 55:1067–1081
- [16] Drew GL, Reed RC, Kakehi K, Rae CMF (2004) Single crystall superalloys: the transition from primary to secondary creep. *Superalloys* 127–136
- [17] Qi D, Wang D, Du K, Qi Y, Lou L, Zhang J, Ye H (2018) Creep deformation of a nickel-based single crystal superalloy under high stress at 1033 K. *J Alloy Compd* 735:813–820
- [18] Yu J, Li JR, Zhao JQ, Han M, Shi ZX, Liu SZ, Yuan HL (2013) Orientation dependence of creep properties and deformation mechanism in DD6 single crystal superalloy at 760 °C and 785 MPa. *Mater Sci Eng A* 560:47–53
- [19] Shi ZX, Li JR, Liu SZ, Wang XG (2014) Creep properties and microstructure evolution of nickel-based single crystal superalloy at different conditions. *Trans Nonferrous Metal Soc* 24:2536–2543
- [20] Pollock TM, Argon AS (1992) Creep resistance of CMSX-3 nickle base superalloy single crystals. *Acta Metall Mater* 4:01–30
- [21] Ullah R, Lu JX, Sang LJ, You XX, Zhang WJ, Zhang YF, Zhang Z (2020) In-situ tensile deformation behavior of as-built laser direct metal deposited Ti–6Al–4V alloy at 200 °C. *J Alloy Compd* 817:152781
- [22] Lu JX, Chang L, Wu J, SangW SK, Zhang YF LJ (2018) In-situ investigation of the anisotropic mechanical properties of laser direct metal deposition Ti6Al4V alloy. *Mater Sci Eng A* 712:199–205
- [23] Wang J, Lu JX, You XX, Rafi U, Sang LJ, Chang L, Zhang YF, Zhang Ze (2019) In-situ comparison of deformation behavior at 23 °C and 650 °C of laser direct melting deposited Ti–6Al–4V alloy. *Mater Sci Eng A* 749:48–55
- [24] Zhang WJ, Lu JX, Wang J, Sang LJ, Ma JY, Zhang YF, Zhang Z (2020) In-situ EBSD study of deformation behavior of inconel 740H alloy at high-temperature tensile loading. *J Alloys Compd* 820:153424
- [25] Sang LJ, Lu JX, Wang J, Ullah R, Sun XC, Zhang YF, Zhang Z (2021) In-situ SEM study of temperature-dependent tensile behavior of Inconel 718 superalloy. *J Mater Sci* 56:16097–16112
- [26] Olaf E, Valerie R (2000) Introduction to texture analysis: macrotexture, microtexture, and orientation mapping, 2nd edn. CRC Press
- [27] Li S, Tian SG, Tao J, Hu ZQ (2006) Influence of pre-compression on microstructure and creep characteristic of a single crystal nickel-base superalloy. *Mater Sci Eng A* 418:229–235
- [28] Webster GA, Pearcey BJ (1967) An interpretation of the effects of stress and temperature on the creep properties of a nickel-base superalloy. *Metal Sci J* 1:97–104
- [29] Xia WS, Zhao XB, Yue L, Zhang Z (2020) A review of composition evolution in Ni-based single crystal superalloys. *J Mater Sci Tech* 44:76–95
- [30] Rae CMF, Rist MA, Cox DC, Reed RC, Matan N (2000) On the primary creep of CMSX-4 superalloy single crystals. *Metal mater trans A* 31:2219–2228
- [31] Rae CMF, Zhang L (2013) Primary creep in single crystal superalloys: some comments on effects of composition and microstructure. *Mater Sci Technol* 25:228–235
- [32] Bürger D, Dlouhý A, Yoshimi K, Eggeler G (2020) On the stress and temperature dependence of low temperature and high stress shear creep in Ni-base single crystal superalloys. *Mater Sci Eng A* 795:139961

- [33] Wang XG, Liu JL, Jin T, Sun XF (2014) Tensile behaviors and deformation mechanisms of a nickel-base single crystal superalloy at different temperatures. *Mater Sci Eng A* 598:154–161
- [34] Wang GL, Liu JL, Liu JD, Wang XG, Zhou YZ, Sun XD, Zhang HF, Jin T (2017) Temperature dependence of tensile behavior and deformation microstructure of a Re-containing Ni-base single crystal superalloy. *Mater Des* 130:131–139
- [35] Li YF, Wang L, Zhang G, Zhang J, Lou LH (2019) Creep anisotropy of a 3rd generation nickel-base single crystal superalloy at 850 °C. *Mater Sci Eng A* 760:26–36

**Publisher's Note** Springer Nature remains neutral with regard to jurisdictional claims in published maps and institutional affiliations.